Available online at www.sciencedirect.com

Manufacturing Letters

Manufacturing Letters 33 (2022) 701–711

50th SME North American Manufacturing Research Conference (NAMRC 50, 2022)

Build surface study of single-layer raster scanning in selective laser melting: Surface roughness prediction using deep learning

Behzad Fotovvati[a,*], Kevin Chou[a]

[a]*Additive Manufacturing Institute of Science and Technology (AMIST), University of Louisville, Louisville, KY 40292, USA*

* Corresponding author. *E-mail address:* b.fotovvati@louisville.edu

Abstract

Selective laser melting (SLM) is a widely used powder-bed fusion additive manufacturing (AM) process for the fabrication of parts from metal powders in a variety of industries such as aerospace, medical, automotive, etc. Despite significant improvements in the design flexibility and mechanical performance, the poor predictability in surface finish, and yet oftentimes with large variability, remains a major challenge in the SLM use. Numerous factors affect the surface roughness of SLM-manufactured parts, which have been reported in the literature, but mostly for bulk samples composed of several layers. In this work, single-layer raster scanning of Ti6Al4V samples are designed and fabricated. The influence of the four most dominant SLM process parameters, i.e., laser power, scanning speed, hatch spacing, and layer thickness on sample surface roughness is thoroughly investigated using a fractional factorial design. Surface roughness data, acquired by white-light interferometry, from 216 data sets are then used to train a machine learning model with the back-propagation method and predict the surface roughness based on the input process parameters. The results show that the laser power is the most significant parameter in determining the top surface roughness of samples. Interestingly, although the investigated samples are single layer raster scanning areas on a solid SLM-built sample with the same parameter set, the layer thickness has a contribution of 10% to 15% in the variations of the surface roughness of the single layers. Furthermore, the machine learning algorithm achieves reasonable predictability, showing a coefficient of determination of 98.8% for a separate 32 testing data set.

Keywords: Selective laser melting; Surface roughness; Machine learning; Artificial neural network; Titanium alloy

1. Introduction

Selective laser melting (SLM), also known as laser-based powder bed fusion (L-PBF) or direct metal laser sintering (DMLS), is one of the most popular types of metal additive manufacturing (AM) that employs metal powders selectively melted in a layer-wise manner by a high-intensity laser beam according to a sliced computer-aided design (CAD) model. SLM is widely used in various industries including medical, automotive, and aerospace. Some examples of these applications include patient-specific metal implants [1], turbine blades [2], engine manifolds [3], and lattice structures [4]. The popularity of this manufacturing technique in such industries is due to many advantages that this method offers: design freedom, reduced manufacturing time, minimized material waste, sustainability benefits, etc. [5]. However, SLM-fabricated parts present several defects in terms of internal pores and surface roughness, which deteriorate the mechanical performance of the components.

Some of the mechanical properties of the SLM parts, such as fracture toughness, can be improved by high-temperature heat treatments, such as hot isostatic pressing (HIP) [6]. While

the HIP treatment significantly reduces internal porosity, its effect on the fatigue resistance of the parts is negligible since fatigue resistance is largely determined by surface defects, which are the potential crack initiation sites, rather than internal porosities [7]. Manipulating surface roughness is also important in medical implants as they need to mimic human bone surface roughness to get the desired interaction between the implant and surrounding tissues. It is imperative, therefore, to be able to manipulate and control the surface roughness of the fabricated parts without requiring additional post-processing processes. Many parameters are involved in the SLM process, e.g., laser beam power and speed, scanning pattern, layer thickness, metal powder size distribution, etc., choice of which significantly affects the process stability and the quality of the parts, including their surface roughness [8–10].

Choosing the appropriate process parameters and their range to manipulate the surface roughness of SLM parts can be utilized through a design of experiment (DoE) technique. A full factorial DoE consists of all the possible combinations of all the values of the parameters. Although knowing the exact behavior of the model for every possible case is an advantage, using a full factorial DoE is sometimes impractical due to the high cost and time associated with samples manufacturing, characterization, and analysis. This is where there is a need for the fractional factorial design of experiments, in which utilizing known properties selectively reduces the number of experiments [11]. An example of employing this statistical method in the SLM process can be seen in a work by Read et al. [12] where the effects of laser power and scan speed on the porosity development in AlSi10Mg alloy samples are investigated. Sing et al. [13] fabricated titanium-tantalum (TiTa) alloy using the SLM process by exploring the influence of different levels of laser power and scanning speed on the relative density and microhardness of fabricated parts. Bang et al. [14] obtained the process conditions to achieve a relative planar density of over 99.5% ± 0.1% for stainless steel 316L samples along with the mechanism of tunable mechanical properties by understanding the correlations between the microstructure, chemical composition, and energy density. Also, the impacts of post-processing conditions can be taken into consideration, such that the effects of heat-treatment parameters, e.g., temperature and time, were investigated alongside the SLM process parameters for Ti6Al4V parts in the literature [15–17].

The combination of DoE approaches with machine learning (ML) methods provides more flexible and powerful techniques for the characterization and optimization of parameters involved in the process. Machine learning methods allow complex pattern recognition and regression analysis to be performed without constructing and solving physical models. A wide range of industries, such as manufacturing, aerospace, and biomedicine, rely on this method to model, predict, and analyze parameter interactions [18–20]. Due to their high processing power and sophisticated architectures, artificial neural networks (ANNs) are the most widely used ML algorithms. An ANN is simply a mathematical model that maps an input space to an output space, and its architecture is composed of an input layer, one or more hidden layers, and an output layer. Properly trained ANNs can model the correlations between the given input and output data and accordingly predict the responses based on unseen input values.

ANNs have been employed in the SLM process in various ways; some of the applications are the design for AM, including topology and material design [21], in-situ process monitoring, including melt pool or powder bed monitoring using optical or acoustic techniques [22–25], and process-property correlation [26,27]. Recently, the process-property correlation application of the ANN models has been extended to the optimization of this process for different materials. An example is the optimization of four SLM process parameters, i.e., laser power, laser scanning speed, layer thickness, and hatch spacing, to achieve a relative density of 99.8% for Ti-6Al-4V parts [28], and that was also extended to include the optimization of the top surface roughness of cubic samples for the same four parameters [29].

Most of the discussed research studies have improved the SLM process parameters and optimized the properties of bulk samples. But to further improve these properties, one may need to dig more into the details of the fabrication and characterization of each layer during the SLM process. One of the main contributions of this work is to investigate the correlations between surface roughness and SLM process parameters and provide predictive models for “single-layer” raster scanning samples, on which there is very limited work in the literature. Single-layer evaluation of samples has a significant value in layer-wise manufacturing processes, e.g., SLM, as the whole part is formed by adding all these single layers. An application of such a predictive model is when it is integrated with an in-situ monitoring system to evaluate the surface of parts, layer by layer, during the manufacturing process and suggests fine-tuning the process parameter to get the desired properties, e.g., to avoid/minimize internal porosity of parts while there are being manufactured.

This paper aims to thoroughly investigate the influence of laser power, scanning speed, hatch spacing, and layer thickness on surface characteristics of single-layer raster scanning of Ti6Al4V samples. A fractional factorial design of experiments (DoE) is employed to cover more factors with wider ranges and more levels to capture the nonlinearities of the responses. To construct a statistically reliable data set, measurements were done on nine areas with different dimensions to have nine replicates for each parameter set and eliminate any possible effect of measurement area size. The surface roughness data collected from the experiments is then used to train a deep learning model to successfully predict the surface roughness of single layer raster scanning based on the input process parameters. The intent is to obtain meaningful correlations between the SLM process parameters and single-layer surface characteristics that can be extended to the interactions between single layers of SLM parts fabricated with different parameter sets, which can play a significant role in realizing the part quality improvement criterion when additional layers are added for fabrication of parts with complex geometries.

2. Experimental Details

2.1. Design of experiments (DoE)

Five levels of power (60 W, 90 W, 120 W, 150 W, and 180 W), five levels of scan speed (500 mm/s, 750 mm/s, 1000 mm/s, 1250 mm/s, and 1500 mm/s), five levels of hatch spacing (50 µm, 75 µm, 100 µm, 125 µm, and 150 µm), and three levels of layer thickness (20 µm, 30 µm, and 40 µm) were used to design the experiment. The ranges for the process parameters were chosen so to revolve around the manufacturer-recommended values to account for the manufacturability of parts. Also, the volumetric energy density absorbed by the metal powders during the SLM process was considered to choose the lowest and highest levels of each parameter. The absorbed volumetric energy density can be estimated by $E = P/(v \cdot h \cdot t)$, where P is laser power, v is scan speed, h is hatch spacing, and t is layer thickness. In general, in an experiment with k factors, having l levels, an l^{k-p} design results in l^{k-p} runs, where p is the reduction factor to reduce the number of experiments. A similar concept can be utilized in a mixture design, where one or some of the factors have different numbers of levels.

Table 1. Fractional factorial DoE of parameter sets used in this study.

Run #	Laser power (W)	Scan speed (mm/s)	Hatch spacing (µm)	Layer thickness (µm)	Volumetric Energy Density (J/mm3)
1	60	500	50	20	120.0
2	60	750	75	40	26.7
3	60	1000	100	30	20.0
4	60	1250	125	20	19.2
5	60	1500	150	40	6.7
6	90	500	75	30	80.0
7	90	750	100	20	60.0
8	90	1000	125	40	18.0
9	90	1250	150	30	16.0
10	90	1500	50	20	60.0
11	120	500	100	40	60.0
12	120	750	125	30	42.7
13	120	1000	150	20	40.0
14	120	1250	50	40	48.0
15	120	1500	75	30	35.6
16	150	500	125	20	120.0
17	150	750	150	40	33.3
18	150	1000	50	30	100.0
19	150	1250	75	20	80.0
20	150	1500	100	40	25.0
21	180	500	150	30	80.0
22	180	750	50	20	240.0
23	180	1000	75	40	60.0
24	180	1250	100	30	48.0
25	180	1500	125	20	48.0

A fractional factorial design with 25 runs was used for this research (Table 1). This design has only 1/15th of the number of experiments in the full factorial design, which requires $5^3 \times 3 = 375$ observations for these numbers of factors and levels. The samples are designed as three 5 mm by 5 mm raster scanning areas for each parameter set on semi-cylinder bases, which were fabricated using default process parameters (laser power: 170 W, scan speed: 1250 mm/s, hatch spacing:100 µm) and were attached to the build plate by support structures. Fig. 1 shows some examples.

2.2. Sample fabrication

An EOS M270 is used to fabricate the designed specimens using Ti-6Al-4V powders from Carpenter Technology Corporation (Philadelphia, PA, USA). The powder particle size distribution was measured using a Microtrac S3500 laser diffraction particle size analyzer (Microtrac MRB, Osaka, Japan) and the results are shown in Fig. 2.

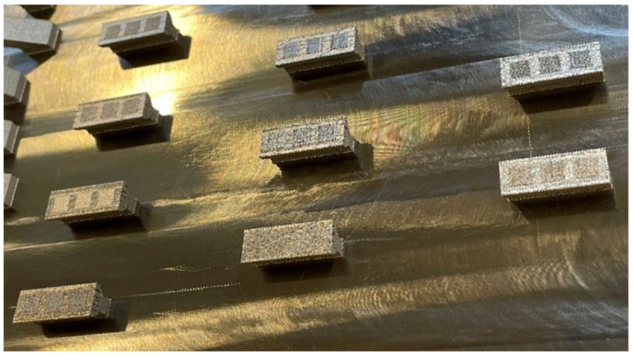

Fig. 1. Examples of fabricated samples on an EOS M270 build plate.

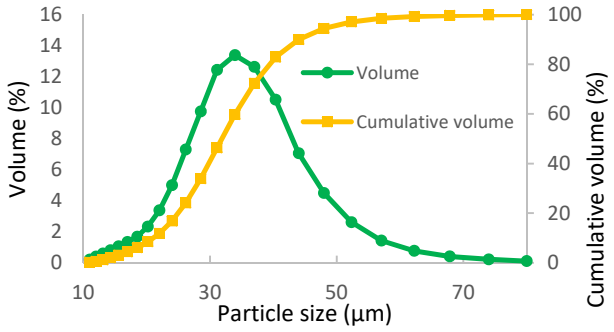

Fig. 2. Ti-6Al-4V powder particle size distribution measured before the first build.

The design of the experiment consisted of three levels of layer thickness. Therefore, three different builds with different layer thicknesses were carried out. Fig. 1 shows some of the samples fabricated with 30 µm layer thickness. After the completion of the build, the specimens were separated from the build plate by cutting the support area with a band saw. Materialise Magics v. 25.0 was used for STL preparation and support generation.

2.3. Surface roughness measurement

A non-contact optical profiler, WYKO NT1100 from Veeco Metrology was used to acquire the surface data of top surfaces based on white light interferometry (WLI). The instrument was calibrated using a 10 µm step-height standard. Vertical scanning interferometry (VSI) measurement mode was chosen with an objective lens of 50X and a 0.5X field of view lens. This gives an effective field of view of 0.25 mm by 0.19 mm. For each parameter set, top surface roughness measurements were done using stitching on nine areas, including six 0.5 mm by 0.5 mm areas and three 1 mm by 1 mm areas to have nine replicates with different area sizes for each sample, resulting in 4.5 mm^2 in total area. Approximate locations of the measured areas of samples are illustrated in Fig. 3. The dark blue arrows in the figure show a schematic of the laser scan directions. The number of scan lines varies in different samples depending on the hatch spacing. Top surface roughness metrics, including S_a and S_v, were measured for each sample. The statistical analysis of this research was carried out using Minitab 20.3 (Minitab Inc., State College, PA, USA).

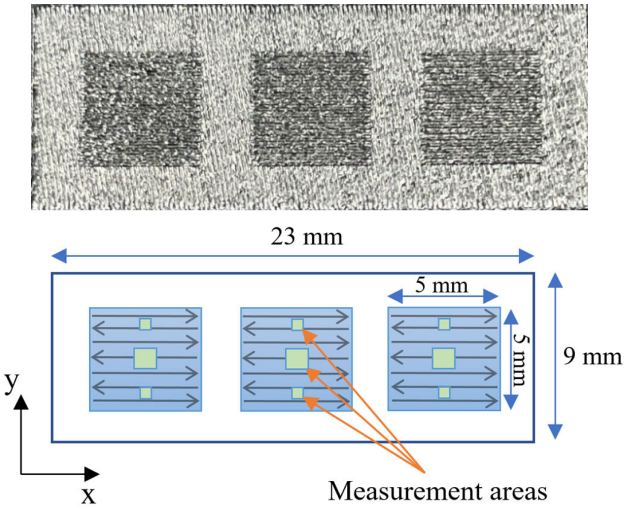

Fig. 3. (Top) actual and (bottom) schematic top views of a sample with three 5 mm by 5 mm raster scans of one parameter set. Nine measurement surface areas (replicates) for each parameter set are shown by green rectangles.

3. Results and discussion

Fig. 4 shows some typical morphologies of top surfaces of samples with different volumetric energy densities (E) resulting in different surface roughness values, on roughness vs. energy density plot, where the correlation of top surface roughness metrics, including S_a and S_v, and volumetric energy density is illustrated. The S_v parameter, which is the depth of the deepest valley in the surface profile, indicates the local extreme situation for crack initiation and is taken into consideration in the literature due to its significance in fatigue life predictions [30,31]. The horizontal and vertical axes in the subfigures (a-d) represent x and y coordinates in mm. The decreasing trend of the surface roughness metrics, i.e., S_a and S_v, with increasing the volumetric surface energy can be observed in Fig. 4. Although the highest energy density, i.e., 240 J/mm^3, (Fig. 4(d)) leads to the lowest top surface roughness, it is not recommended for part manufacturing, because of gas pores and micro-cracks formed due to overheating at these energy densities. These pores decrease the fractional density of the part and cause the optimum energy density to be at the local extrema in the profiles of the surface roughness and fractional densities at 40–60 J/mm^3 for this material [32]. Also, microcracks can act as crack initiators under dynamic loading. Examples are shown in Fig. 4(d).

As it is discussed earlier, the volumetric energy density is a function of the SLM process parameters, i.e., laser power, scan speed, hatch spacing, and layer thickness. So, to investigate the contribution of each factor to the total variations in the surface roughness values, an analysis of variance (ANOVA) is performed with 95% confidence, for S_a and S_v, and the results are presented in Table 2 and Table 3, respectively. Moreover, to investigate the correlations between the top surface roughness and the process parameters, main effect plots are presented in Fig. 5.

The significance of parameters can be comprehended by comparing the P-values in ANOVA. Generally, smaller p-values indicate greater statistical incompatibility with the null hypothesis, implying a greater significance of the parameter. According to Table 2 and Table 3, all the parameters show great significance in determining the response parameters, i.e., S_a and S_v. So, to compare the level of contribution of each factor, the percent contribution of them was calculated by dividing the sum of squares for each factor by the total sum of squares of all factors and multiplying the result by 100 [33].

The ANOVA results show that the laser power and layer thickness are the most and the least significant factors, respectively, among the other parameters; however, it should be noted that the chosen value range for the layer thickness is smaller than the other parameters. All the parameter ranges are designed, from the lowest to the highest level, to have a similar effect on the energy density, i.e., increasing it to the order of three, except for the layer thickness that changes the energy density in the order of two; and that is due to the limitations of the number of experiments and avoiding levels far from the recommended values. So, considering this limitation for the layer thickness, it might have a similar level of significance to the laser power if the parameter range could be extended to 60 µm, as it is reported elsewhere for the same material [34].

Table 2. ANOVA for main effects of parameters on S_a.

Source	DoF	Adjusted sum of squares	Adjusted mean square	F-value	P-value	Contribution %
Laser power	4	4910.2	1227.6	148.33	0.000	45.1
Scan speed	4	2212.2	553.1	66.83	0.000	20.3
Hatch spacing	4	2564.0	641.0	77.45	0.000	23.6
Layer thickness	2	1198.0	599.0	72.38	0.000	11.0

Table 3. ANOVA for main effects of parameters on S_v.

Source	DoF	Adjusted sum of squares	Adjusted mean square	F-value	P-value	Contribution %
Laser power	4	26621	6655.3	78.94	0.000	34.5
Scan speed	4	21243	5310.8	62.99	0.000	27.5
Hatch spacing	4	18310	4577.5	54.30	0.000	23.7
Layer thickness	2	11010	5505.1	65.30	0.000	14.3

The results presented in Fig. 5 suggest using the highest energy density, which is obtained by the combination of the highest level of laser power and the lowest levels of scan speed, hatch spacing, and layer thickness, leads to obtaining the smallest roughness values for the top surface roughness of SLM parts, which is in line with the results presented in Fig. 4; Nevertheless, when choosing the desired layer thickness value for manufacturing a part using the SLM process, other factors, such as manufacturing time, the powder size distributions, and powder bed distortion due to the inert gas flow, must be taken into consideration, as well.

A possible interpretation for this behavior at higher energy densities may be the gravitational force that smoothens the melt tracks on the top surfaces. It was observed that increasing the energy density increases the top surface quality in terms of roughness. Still, it cannot be concluded that any changes in any of the process parameters that increase the energy density, will play a role in decreasing the surface roughness. The two parameters that did not show a sustained increment/decrement within their ranges were scanning speed and hatch spacing. As it is depicted in Fig. 5(a), the maximum S_a values happen at a scan speed of 1000 mm/s and hatch spacing of 125 µm. Top surface roughness increases with increasing hatch spacing up to 125 µm because, at low hatch spacing values, the overlaps of adjacent melt tracks flatten the melt beads and create a smooth surface. Increasing the hatch spacing and moving melt tracks apart from each other, forms deep valleys between the tracks that significantly increases the surface roughness; however, since single layer scanning is being investigated in this research, and the previous layer belongs to a base fabricated using the manufacturer-recommended process parameters, which is not optimized solely for the top surface roughness, when the melt tracks move apart, after some point, 125 µm in this case, the previous layer incorporates more in surface roughness measurement of these samples, as it is illustrated in Fig. 6. Therefore, in the study of single-layer raster scanning, increasing hatch spacing after some point highlights the role of the previous layer in surface roughness determination of the top surface. So, a high-energy parameter set, e.g., P = 180 W, v = 750 mm/s, h = 50 µm, t = 20 µm, which results in the lowest surface roughness (see Figure 4) may be used as the top surface of the bases before depositing the single-layer samples.

Fig. 5 also suggests that decreasing layer thickness increases the top surface quality, for both S_a and S_v metrics. Debroy et al. [35] reported the same behavior for surface roughness of SLM parts, regardless of the material. Therefore, the smallest possible layer thickness is recommended in the SLM process to minimize the surface roughness; however, to determine a lower limit for the layer thickness, other above-mentioned factors need to be taken into account.

In addition to the ANOVA for the main effects of the parameters, an ANOVA for the parameters and their two-way interactions was performed to evaluate the interactions of the parameters in determining the top surface response. Table 4 presents the results of the ANOVA for main effects and interactions of parameters on S_a. Also, Fig. 7 shows the process parameters' interaction for top surface roughness assessment S_a.

The last column of Table 4 shows that even by considering the parameters' interactions, laser power is still the most dominant factor among all the other parameters and their interactions. The contribution of all the two-way interactions of the parameters, except for laser power and layer thickness interaction, turned out to be negligible compared to the main effects of the parameters. The dependence of laser power and layer thickness can be also observed at the top right corner grid of Fig. 7, where the row of laser power intersects with the column of layer thickness.

Fig. 7 shows how the relationship between one categorical factor and a continuous response depends on the value of the second categorical factor. This plot shows the means for the levels of one factor on the x-axis and a separate line for each level of another factor. In this Fig., each row/column is assigned to one parameter. In other words, laser power (W), scan speed (mm/s), hatch spacing (µm), and layer thickness (µm) are assigned to the first, second, third, and fourth row/column, respectively. The interaction of each two parameters is presented in the intersection block of the row and column of those two parameters. For instance, the top right corner of Fig. shows the interaction of laser power (row) and layer thickness (column). It can be seen in this Fig. that at lower levels of power, i.e., 60 W and 90 W, increasing the layer thickness increases the surface roughness significantly; however, at higher laser power values, changing layer thickness does not have any significant effects on the roughness. In other words, at high powers, surface roughness is not a function of layer thickness. A possible reason might be that the laser beam at lower powers can melt the entire layer when it is thin, but it has limited penetration depth at thicker layers; Nonetheless, high-power laser beams have full penetration regardless of the layer thickness.

Generally, on an interaction plot, parallel lines indicate no interaction between the two parameters, however, nonparallel lines show an interaction between the two parameters. The more nonparallel the lines are, the greater the strength of the interaction.

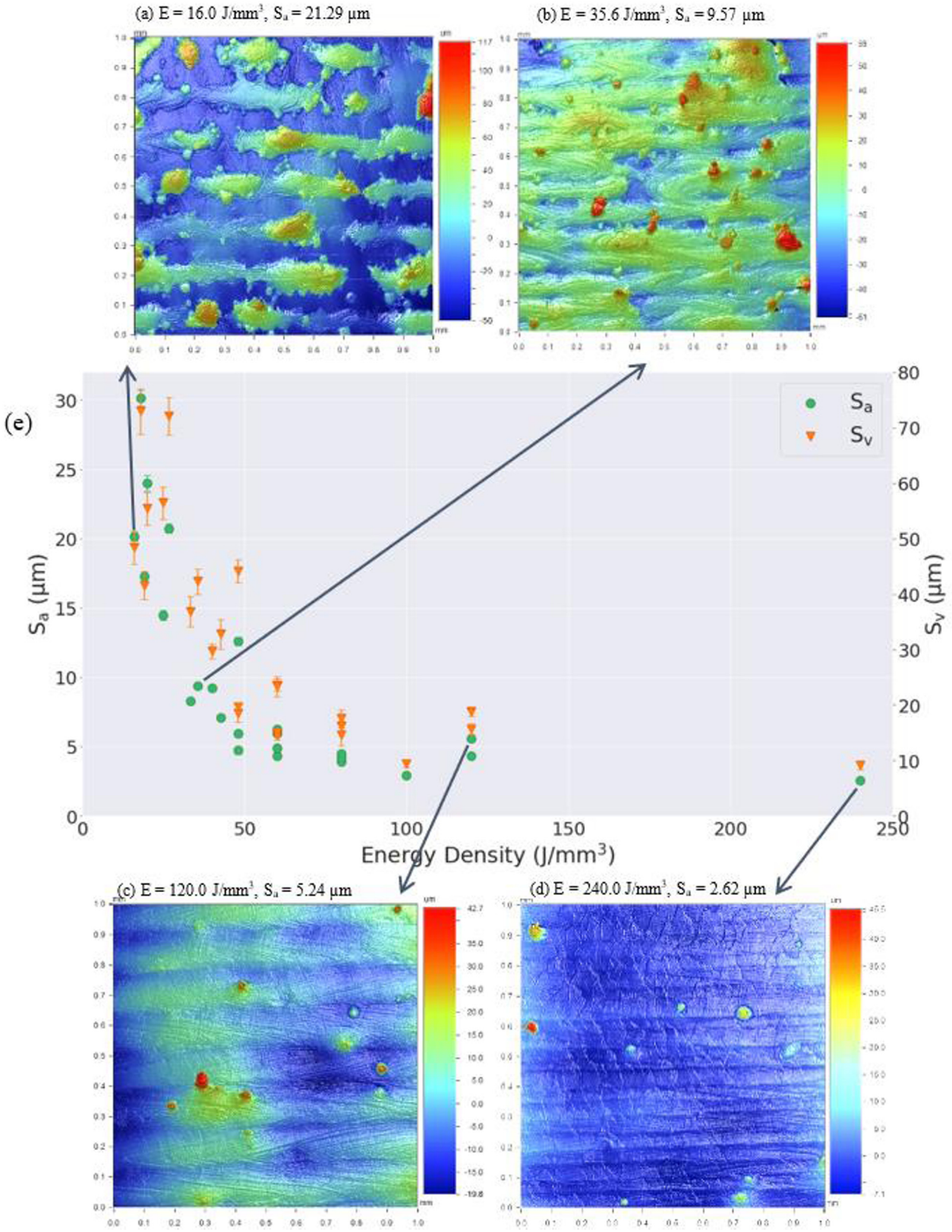

Fig. 4. Typical morphology of top surfaces for different parameter sets (a-d) showed on the top surface roughness (Sa) vs. energy density plot (e). The parameters are (a) P = 90 W, v = 1250 mm/s, h = 150 µm, t = 30 µm, (b) P = 120 W, v = 1500 mm/s, h = 75 µm, t = 30 µm, (c) P = 150 W, v = 500 mm/s, h = 125 µm, t = 20 µm, (d) P = 180 W, v = 750 mm/s, h = 50 µm, t = 20 µm.

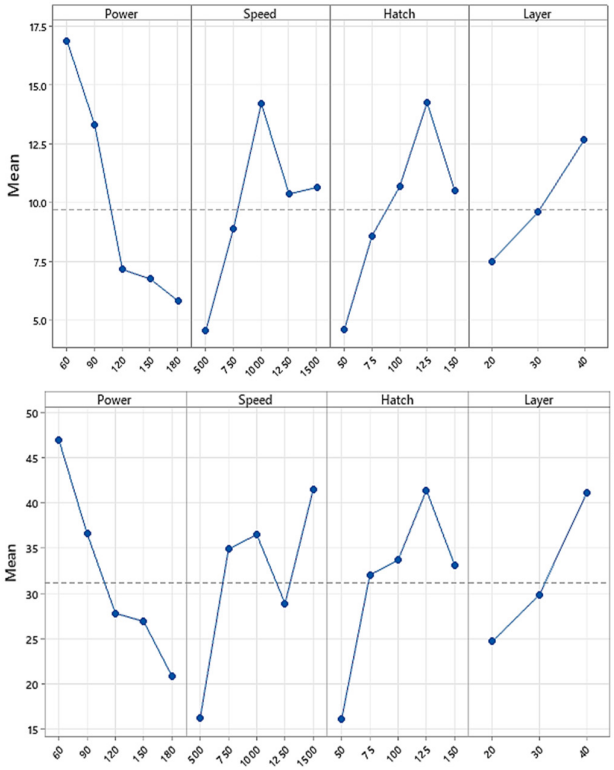

Fig. 5. Main effects plots for surface parameters: (Top) S_a, and (Bottom) S_v.

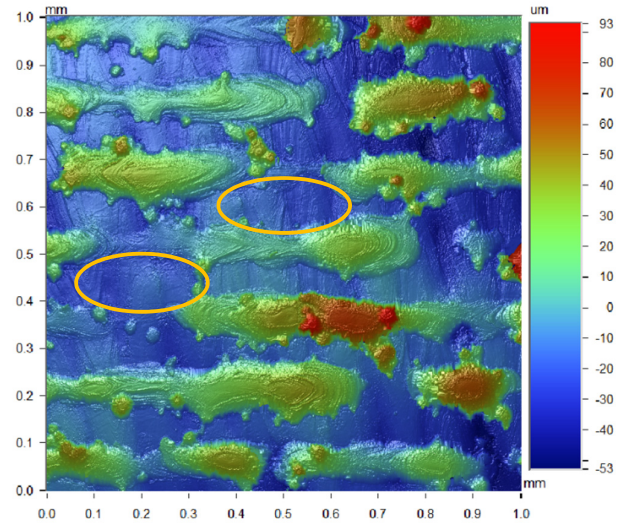

Fig. 6. A sample with a large hatch spacing (h = 150 µm) showing the contribution of the previous layer in the surface roughness measurement of the top layer. Other process parameters for this sample are P = 90 W, v =1250 mm/s, and t = 30 µm. Examples of the regions with the exposed previous layer are shown in orange ellipses.

Table 4. ANOVA for main effects and interactions of parameters on S_v. *P* is laser power, *v* is scan speed, *h* is hatch spacing, and *t* is layer thickness.

Source	DoF	Adjusted sum of squares	Adjusted mean square	F-value	P-value	Contribution %
P	1	4910.2	1227.6	148.33	0.000	45.1
v	1	2212.2	553.1	66.83	0.000	20.3
h	1	2564.0	641.0	77.45	0.000	23.6
t	1	171.9	171.94	19.94	0.000	1.7
P . *v*	1	36.8	36.84	4.27	0.040	0.4
P . *h*	1	1206.7	1206.72	139.95	0.000	11.7
P . *t*	1	373.7	373.66	43.33	0.000	3.6
v . *h*	1	164.3	164.30	19.06	0.000	1.6
v . *t*	1	107.2	107.16	12.43	0.001	1.0
h . *t*	1	171.9	171.94	19.94	0.000	1.7

4. Artificial neural network (ANN)

In this research, the input layer of the ANN is designed with four neurons corresponding to the four SLM process parameters, i.e., *P*, *v*, *h*, and *t*, and the output layer has one neuron to predict the top surface S_a value. A total of 216 data sets were split into 85% training and 15% testing data. K-fold cross-validation with K = 6 was used to again break the training set into ~85% training and ~15% cross-validation sets. Since the input parameters have different ranges, a normalization preprocessing was performed on the input data. The back-propagation method was employed for training the model. In this method, gradients are computed iteratively for each layer by applying the mathematical chain rule [36]. The objective of the training process is to optimize the hyperparameters, e.g., weights and bias values, of the model by minimizing the loss function. An Adam optimizer is used for this purpose. In the beginning, the weights are distributed randomly to the nodes. Based on the known inputs and outputs of the training data, the model calculates and compares its resulting outputs against the desired outputs and then adjusts its weights based on errors propagated back into it. This process is repeated until the loss is minimized. The learning rate, which is the amount that the weights are updated each time during training, was set to 0.0005.

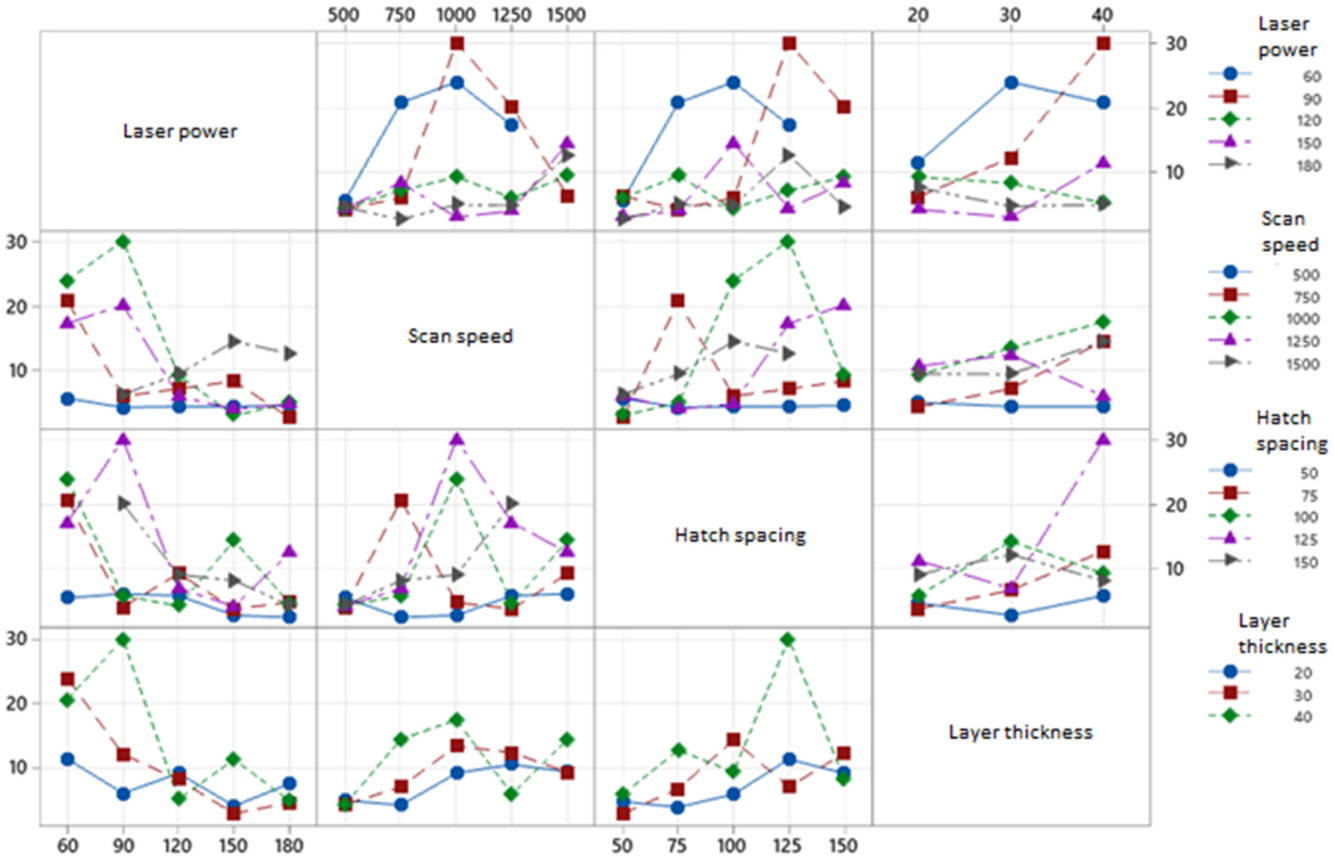

Fig. 7. Parameters' interaction plots for S_a. All vertical axes show S_a values in µm.

After testing several networks with different numbers of hidden layers and nodes, the architecture with two hidden layers with 200 and 150 neurons in the first and second layers, respectively, showed the best performance in terms of prediction accuracy. To avoid overfitting, where the model has high accuracy on the training data but is not likely to perform well on the testing data, the weight regularization (weight decay) [37] and the dropout methods [38] are used. Weight regularization penalizes the model during training based on the magnitude of the weights and prevents the weights from growing too large by adding a term to the loss function. A Ridge regression (L2) regularization was used for this model:

$$Loss = \frac{1}{N}\sum_{i=1}^{N}\left(\hat{Y}_i - Y_i\right)^2 + \lambda\sum_{i=1}^{N}\theta_i^2$$

where N is the number of datasets, Y and $\hat{Y}$ are the predicted and actual responses, respectively, and θ is the weight vector. λ is a regularization parameter determining the extent of the penalization of large weights in the model and was set to be 0.02 in this research. In addition to weight regularization, the dropout method, in which units are randomly dropped from the layers during training, was employed to avoid overfitting. By treating the layers as layers with fewer nodes and connections to prior layers, this approach breaks up situations where the layers co-adapt to correct mistakes from prior layers, thus making the model more robust. In this research, the probabilities of retaining a unit in the first and second hidden layers were 0.45 and 0.5, respectively.

Rectified Linear Unit (ReLU) activation functions were used for the hidden layers and a linear activation function was utilized for the output layer. The ANN training, testing, and evaluations are performed using Python 3.8.8 in the PyCharm 2021.1.2 environment and the TensorFlow library. Mean square error (MSE) and r-squared (the coefficient of determination) were used to assess the prediction accuracy and performance of the model. $MSE = 1/n\sum\left(Y_i - \hat{Y}_i\right)^2$ The ANN results and performance is summarized in Table 5 and Fig. 8.

This model now can predict the surface roughness of any combinations of the process parameters. To predict the extreme cases according to the main effect plots (Fig. 5), they were fed into the trained network to see what the maximum and minimum S_a values are obtainable in this range of processing parameters. Fig. 5 suggests that the following parameter set P = 180 W, v = 500 mm/s, h = 50 µm, and t = 20 µm leads to the highest surface quality, and using P = 60 W, v = 1000 mm/s, h = 125 µm, and t = 40 µm, results in the maximum surface roughness value. These extreme cases were predicted by the trained model as S_a = 1.08 µm and S_a = 38.33 µm, respectively. Note that these values may not be achievable due to the limitations of the manufacturability of some parameter combinations as discussed earlier in section 2.1.

A linear regression model was used for comparison purposes of the ANN results. The linear regression equation was obtained as:

$$Sa = -2.08 - 0.10918\,P + 0.008097\,v + 0.09178\,h + 0.2833\,t$$

where P is the laser power, v is the scanning speed, h is the hatch spacing, and t is the layer thickness. The mean square error and the coefficient of determination of the predicted values by this linear regression model were 18.6874 (compared to 0.6718 for the ANN) and 65.26% (compared to 98.79% for the ANN), respectively.

Table 5. The ANN performance in terms of MSE and r-squared for testing and training data.

	Mean square error	Coefficient of determination
Training data	0.6718	98.79 %
Testing data	0.5264	98.82 %

5. Conclusions

To gain a deeper understanding of how single layer formation is influenced by the SLM process parameters, this paper thoroughly investigates the effects of laser power, scanning speed, hatch spacing, and layer thickness on surface characteristics of single-layer raster scanning of Ti6Al4V samples fabricated by SLM. A fractional factorial design of experiments (DoE) is employed to cover more factors with wider ranges and more levels so as to capture the nonlinearities of the responses. Measurements were done on nine areas of varying sizes for each parameter set to construct a statistically reliable data set and to eliminate any possible effect of the size of the measurement area. The single-layer raster scanning surface roughness data is then used to train a machine learning model to successfully predict the responses based on the input process parameters. Such an ML model can be integrated with an in-situ monitoring system to evaluate the surface of parts, layer by layer, during the manufacturing process and suggests fine-tuning the process parameter to get the desired properties, e.g., to avoid/minimize internal porosity of parts while there are being manufactured. The analyses and results show that:

- Both S_a and S_v metrics of the top surface decrease with increasing the volumetric energy density.
- Among the investigated parameters, laser power and layer thickness have the most and least significant effects on the top surface roughness, respectively.
- The combination of the highest level of laser power and the lowest levels of scan speed, hatch spacing, and layer thickness, e.g., the highest energy density (240 J/mm3), results in the smallest roughness values for the top surface roughness of SLM parts. However, too high energy densities lead to the formation of other types of defects, such as surface cracks.

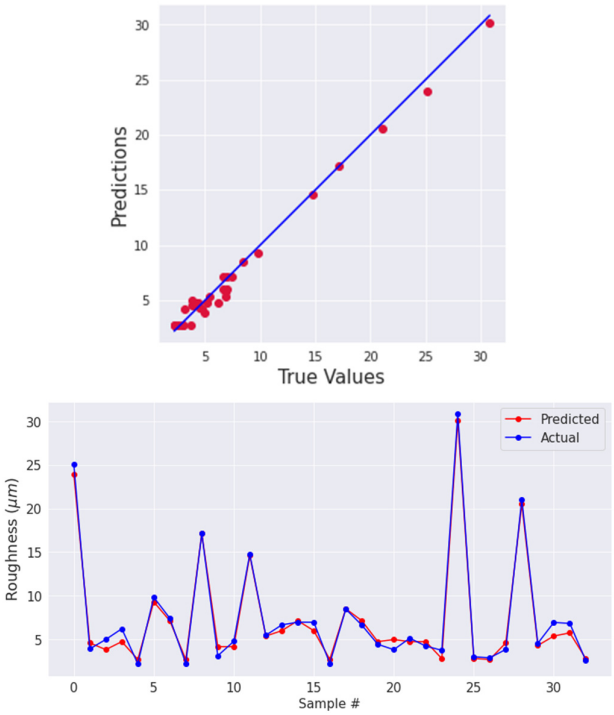

Fig. 8. ANN performance on the testing data in terms of actual vs predicted values.

- Decreasing the layer thickness increases the top surface quality, for both S_a and S_v metrics; however, other factors, such as manufacturing time, powder size distributions, and powder-bed distortion caused by inert gas flow, are recommended to be taken into account, when determining a lower limit for the layer thickness.
- Higher laser power values diminish the effects of layer thickness on the top surface roughness.
- Top surface roughness increases with increasing hatch spacing up to 125 µm. Increasing the hatch spacing more to 150 µm forms deep valleys between the tracks that should significantly increase the surface roughness; however, when the melt tracks move apart, the previous layer, which is smoother, incorporates more in surface roughness measurement of these samples and results in lower values for both S_a and S_v.
- Except for the laser power and layer thickness interaction, the two-way interactions of all the other parameters are negligible in determining the top surface roughness values.
- An artificial neural network was trained using some of the experimental data collected throughout this research and was tested successfully with a separate data set, showing a coefficient of determination of 98.8% for the testing data set.

Acknowledgments

This research was supported by the National Science Foundation (NSF) under Grant Number # 1921263.

References

[1] Li J, Hu J, Zhu Y, Yu X, Yu M, Yang H. Surface roughness control of root analogue dental implants fabricated using selective laser melting. Additive Manufacturing 2020;34:101283. https://doi.org/10.1016/J.ADDMA.2020.101283.

[2] Torres-Carrillo S, Siller HR, Vila C, López C, Rodríguez CA. Environmental analysis of selective laser melting in the manufacturing of aeronautical turbine blades. Journal of Cleaner Production 2020;246:119068. https://doi.org/10.1016/J.JCLEPRO.2019.119068.

[3] Sajedi Z, Casati R, Poletti MC, Skalon M, Vedani M. Thermal fatigue testing of laser powder bed fusion (L-PBF) processed AlSi7Mg alloy in presence of a quasi-static tensile load. Materials Science and Engineering: A 2020;789:139617. https://doi.org/10.1016/J.MSEA.2020.139617.

[4] Zhang L, Song B, Fu JJ, Wei SS, Yang L, Yan CZ, et al. Topology-optimized lattice structures with simultaneously high stiffness and light weight fabricated by selective laser melting: Design, manufacturing and characterization. Journal of Manufacturing Processes 2020;56:1166–77. https://doi.org/10.1016/J.JMAPRO.2020.06.005.

[5] Mehrpouya M, Vosooghnia A, Dehghanghadikolaei A, Fotovvati B. The benefits of additive manufacturing for sustainable design and production. Sustainable Manufacturing 2021;29-59. doi:10.1016/B978-0-12-818115-7.00009-2

[6] Liverani E, Lutey AHA, Ascari A, Fortunato A. The effects of hot isostatic pressing (HIP) and solubilization heat treatment on the density, mechanical properties, and microstructure of austenitic stainless steel parts produced by selective laser melting (SLM). International Journal of Advanced Manufacturing Technology 2020;107:109–22. https://doi.org/10.1007/S00170-020-05072-9/FIGURES/17.

[7] Fotovvati B, Namdari N, Dehghanghadikolaei A. Fatigue performance of selective laser melted Ti6Al4V components: State of the art. Materials Research Express 2018;6:012002.

[8] Hu Z, Qi Y, Nagarajan B, Nie X, Zhang H, Zhu H, et al. Top surface roughness evolution during selective laser melting of AlCu5MnCdVA aluminum alloy. Journal of Manufacturing Processes 2021;64:1180–95. https://doi.org/10.1016/J.JMAPRO.2021.01.051.

[9] Yang T, Liu T, Liao W, MacDonald E, Wei H, Chen X, et al. The influence of process parameters on vertical surface roughness of the AlSi10Mg parts fabricated by selective laser melting. Journal of Materials Processing Technology 2019;266:26–36. https://doi.org/10.1016/J.JMATPROTEC.2018.10.015.

[10] Tian Y, Tomus D, Rometsch P, Wu X. Influences of processing parameters on surface roughness of Hastelloy X produced by selective laser melting. Additive Manufacturing 2017;13:103–12. https://doi.org/10.1016/J.ADDMA.2016.10.010.

[11] Gunst RF, Mason RL. Fractional factorial design. Wiley Interdisciplinary Reviews: Computational Statistics 2009;1:234–44. https://doi.org/10.1002/WICS.27.

[12] Read N, Wang W, Essa K, Attallah MM. Selective laser melting of AlSi10Mg alloy: Process optimisation and mechanical properties development. Materials & Design (1980-2015) 2015;65:417–24. https://doi.org/10.1016/J.MATDES.2014.09.044.

[13] Sing SL, Wiria FE, Yeong WY. Selective laser melting of titanium alloy with 50 wt% tantalum: Effect of laser process parameters on part quality. International Journal of Refractory Metals and Hard Materials 2018;77:120–7. https://doi.org/10.1016/J.IJRMHM.2018.08.006.

[14] Bang GB, Kim WR, Kim HK, Park HK, Kim GH, Hyun SK, et al. Effect of process parameters for selective laser melting with SUS316L on mechanical and microstructural properties with variation in chemical composition. Materials & Design 2021;197:109221. https://doi.org/10.1016/J.MATDES.2020.109221.

[15] Khorasani AM, Gibson I, Awan US, Ghaderi A. The effect of SLM process parameters on density, hardness, tensile strength and surface quality of Ti-6Al-4V. Additive Manufacturing 2019;25:176–86. https://doi.org/10.1016/J.ADDMA.2018.09.002.

[16] Khorasani AM, Gibson I, Ghaderi A, Mohammed MI. Investigation on the effect of heat treatment and process parameters on the tensile behaviour of SLM Ti-6Al-4V parts. The International Journal of Advanced Manufacturing Technology 2018 101:9 2018;101:3183–97. https://doi.org/10.1007/S00170-018-3162-8.

[17] Khorasani AM, Gibson I, Ghasemi AH, Ghaderi A. A comprehensive study on variability of relative density in selective laser melting of Ti-6Al-4V. Https://DoiOrg/101080/1745275920191614198 2019;14:349–59. https://doi.org/10.1080/17452759.2019.1614198.

[18] Xing W, Lyu T, Chu X, Rong Y, Lee CG, Sun Q, et al. Recognition and classification of single melt tracks using deep neural network: A fast and effective method to determine process windows in selective laser melting. Journal of Manufacturing Processes 2021;68:1746–57. https://doi.org/10.1016/J.JMAPRO.2021.06.076.

[19] Park HS, Nguyen DS, Le-Hong T, van Tran X. Machine learning-based optimization of process parameters in selective laser melting for biomedical applications. Journal of Intelligent Manufacturing 2021:1–16. https://doi.org/10.1007/S10845-021-01773-4/TABLES/6.

[20] Stolt R, Elgh F. Introducing design for selective laser melting in aerospace industry. Journal of Computational Design and Engineering 2020;7:489–97. https://doi.org/10.1093/JCDE/QWAA042.

[21] Hong R, Zhang L, Lifton J, Daynes S, Wei J, Feih S, et al. Artificial neural network-based geometry compensation to improve the printing accuracy of selective laser melting fabricated sub-millimetre overhang trusses. Additive Manufacturing 2021;37:101594. https://doi.org/10.1016/J.ADDMA.2020.101594.

[22] Fang Q, Tan Z, Li H, Shen S, Liu S, Song C, et al. In-situ capture of melt pool signature in selective laser melting using U-Net-based convolutional neural network. Journal of Manufacturing Processes 2021;68:347–55. https://doi.org/10.1016/J.JMAPRO.2021.05.052.

[23] Tan Z, Fang Q, Li H, Liu S, Zhu W, Yang D. Neural network based image segmentation for spatter extraction during laser-based powder bed fusion processing. Optics & Laser Technology 2020;130:106347. https://doi.org/10.1016/J.OPTLASTEC.2020.106347.

[24] Wang L, Chen X, Henkel D, Jin R. Pyramid Ensemble Convolutional Neural Network for Virtual Computed Tomography Image Prediction in a Selective Laser Melting Process. Journal of Manufacturing Science and Engineering 2021;143. https://doi.org/10.1115/1.4051077.

[25] Shevchik SA, Kenel C, Leinenbach C, Wasmer K. Acoustic emission for in situ quality monitoring in additive manufacturing using spectral convolutional neural networks. Additive Manufacturing 2018;21:598–604. https://doi.org/10.1016/J.ADDMA.2017.11.012.

[26] Tran HC, Lo YL. Systematic approach for determining optimal processing parameters to produce parts with high density in selective laser melting process. International Journal of Advanced Manufacturing Technology 2019;105:4443–60. https://doi.org/10.1007/S00170-019-04517-0/TABLES/7.

[27] Marrey M, Malekipour E, El-Mounayri H, Faierson EJ. A Framework for Optimizing Process Parameters in Powder Bed Fusion (PBF) Process Using Artificial Neural Network (ANN). Procedia Manufacturing 2019;34:505–15. https://doi.org/10.1016/J.PROMFG.2019.06.214.

[28] Nguyen DS, Park HS, Lee CM. Optimization of selective laser melting process parameters for Ti-6Al-4V alloy manufacturing using deep learning. Journal of Manufacturing Processes 2020;55:230–5. https://doi.org/10.1016/J.JMAPRO.2020.04.014.

[29] Park HS, Nguyen DS, Le-Hong T, van Tran X. Machine learning-based optimization of process parameters in selective laser melting for biomedical applications. Journal of Intelligent Manufacturing 2021:1–16. https://doi.org/10.1007/S10845-021-01773-4/TABLES/6.

[30] Liang X, Robert C, Hor A, Morel F. Numerical investigation of the surface and microstructure effects on the high cycle fatigue performance of additive manufactured stainless steel 316L. International Journal of Fatigue 2021;149:106273. https://doi.org/10.1016/J.IJFATIGUE.2021.106273.

[31] Martin-Meizoso A, Martinez-Esnaola JM, Arrazola PJ, Linaza A. Surface machining condition and fatigue life on Inconel 718. Procedia Structural Integrity 2018;13:1609–14. https://doi.org/10.1016/J.PROSTR.2018.12.339.

[32] Attarzadeh F, Fotovvati B, Fitzmire M, Asadi E. Surface roughness and densification correlation for direct metal laser sintering. The International

Journal of Advanced Manufacturing Technology 2020;107:2833–42. https://doi.org/10.1007/s00170-020-05194-0.

[33] Bartolomeu F, Faria S, Carvalho O, Pinto E, Alves N, Silva FS, et al. Predictive models for physical and mechanical properties of Ti6Al4V produced by Selective Laser Melting. Materials Science and Engineering: A 2016;663:181–92. https://doi.org/10.1016/J.MSEA.2016.03.113.

[34] Fotovvati B, Balasubramanian M, Asadi E. Modeling and Optimization Approaches of Laser-Based Powder-Bed Fusion Process for Ti-6Al-4V Alloy. Coatings 2020;10:1104. https://doi.org/10.3390/coatings10111104.

[35] DebRoy T, Wei HL, Zuback JS, Mukherjee T, Elmer JW, Milewski JO, et al. Additive manufacturing of metallic components – Process, structure and properties. Progress in Materials Science 2018;92:112–224. https://doi.org/10.1016/J.PMATSCI.2017.10.001.

[36] Rumelhart DE, Hinton GE, Williams RJ. Learning representations by back-propagating errors. Nature 1986 323:6088 1986;323:533–6. https://doi.org/10.1038/323533a0.

[37] Zur RM, Jiang Y, Pesce LL, Drukker K. Noise injection for training artificial neural networks: A comparison with weight decay and early stopping. Medical physics 2009, 36(10), 4810-4818.

[38] Srivastava N, Hinton G, Krizhevsky A, Sutskever I, Salakhutdinov R. Dropout: a simple way to prevent neural networks from overfitting. The journal of machine learning research 2014, 15(1), 1929-1958.